

---

# Implicit Data Synthesis for Contrastive Unsupervised Data Augmentation

---

**Patrick Kage**

School of Informatics  
The University of Edinburgh  
Edinburgh, Scotland EH8 9AB UK  
p.kage@ed.ac.uk

**Trevor Hedges**

Massachusetts Institute of Technology Lincoln Laboratory  
Lexington, MA 02421 USA  
trevor.hedges@ll.mit.edu

**N. Siddharth**

School of Informatics  
The University of Edinburgh  
Edinburgh, Scotland EH8 9AB UK  
n.siddharth@ed.ac.uk

**Pavlos Andreadis**

School of Informatics  
The University of Edinburgh  
Edinburgh, Scotland EH8 9AB UK  
pavlos.andreadis@ed.ac.uk

## Abstract

Scientific observations generate large quantities of unlabeled data which is laborious to hand-label, making unsupervised learning techniques valuable for processing datasets. Among these approaches, contrastive learning provides a convenient mechanism for extracting structural representations from unannotated datasets. For natural imagery, the general approach is to use a variety of data-space augmentation methods in order to generate synthetic samples; however, for scientific observations data-space perturbations can fundamentally alter the underlying data. Our proposed method is to generate contrastive samples by perturbing the network weights rather than the underlying data, thus more closely preserving the structure of the data. We demonstrate this technique using a SimCLR-based pipeline applied over radar observations of meteors, and show performance gains under matched protocols.

## 1 Introduction

The advent of modern machine learning techniques provides scientists powerful tools for the processing of experiment data, allowing for analyses such as classification, clustering, anomaly detection, semantic segmentation, and more. However, the application of such tools is limited by the core drawback of supervised learning: the necessity of large quantities of labeled data with which to train machine learning models. In scientific domains, the creation of large, high-quality datasets is extremely labor-intensive, requiring domain experts to tediously label thousands of samples by hand. To combat this, the field of *unsupervised learning* has emerged, which allows for label-free analysis of datasets—skirting the need for human labeling by leveraging the inherent properties of the data to create an analysis pipeline. Within this field, *unsupervised representation learning* is a common task, which aims to distill high-dimensional data into low-dimensional vectors capturing semantic information about the sample, allowing for easier downstream analysis [15, 3].

Contrastive learning techniques are a natural fit for creating unsupervised representation learning systems as they strive to learn common features between similar samples while separating dissimilar samples. This yields a system which is able to cluster semantically similar samples in feature space without needing a class assignment—only a metric of how similar samples are to each other [12]. In general, these systems work by augmenting a sample  $\mathbf{x}$  to create a set of (typically two) positive samples<sup>1</sup>  $\{\hat{\mathbf{x}}_1, \hat{\mathbf{x}}_2, \dots\}$  with the property that these two samples share the same underlying class assignment. These samples are then projected into latent space by an encoder network and projection network which attempts minimize the space between positive samples and the rest of the batch (negative samples) [12, 3], yielding a system capable of semantically embedding unlabeled samples into a latent space.

A core component of the success of contrastive learning techniques is the data augmentation strategy, *i.e.* the ability for the system to generate positive samples  $\hat{\mathbf{x}}$  that differ from the original sample  $\mathbf{x}$ , but map to the same location in the final embedding space. It has been shown that effective augmentations are key to a robust embedding system [12]. This brings us to the key problem addressed by this paper: while many strategies exist for natural imagery [20], creating augmentations for non-image data requires bespoke augmentations which take into account what features of the data can be changed without fundamentally altering its class—a challenging task.

This difficulty is particularly pronounced when analyzing meteor data from scientific radars such as the Jicamarca Radio Observatory (JRO) in Lima, Peru. These extremely sensitive radar facilities can detect thousands of tiny meteors (originating from dust particles in space) entering Earth’s atmosphere per hour [10], yielding enormous datasets. The most common meteor radar signatures observed by JRO, known as *head echoes*, provide insights into atmospheric composition and formation of the solar system, yet the process of manually labeling radar data is prohibitively time-consuming [11]. Furthermore, standard natural imagery augmentations cannot be trivially applied to radar data without corrupting the underlying physical phenomena represented in the signal. Radar observations of meteors are processed as two-dimensional datasets where the horizontal axis represents time and the vertical axis altitude, so the spatial axes are not interchangeable. A meteor’s apparent velocity is given by the slope of its trajectory in this plane: arbitrary rotations rescale that velocity, and reflections invert its sign, producing samples in which meteors appear to ascend through the atmosphere. Pixel intensities are similarly tied to calibrated signal-to-noise ratios that represent the size of a meteor rather than perceptual quantities, so color jitter augmentations are not physically meaningful either.

To address this, we propose using *implicit data synthesis* (IDS). Rather than modifying the data in data space, we instead add a bounded noise term to a subset of the layers of the encoder network, effectively augmenting the data in representation space. This approach has previously shown efficacy in anomaly detection via Wasserstein-Distributed Outlier Exposure (W-DOE) [24], where a similar approach to IDS was utilized to expand the out-of-distribution dataset. In this work, we adapt this theory to contrastive learning, creating a robust unsupervised representation learning pipeline applicable to meteor radar data and other scientific observations. We show that IDS alone is as effective as data-space augmentations for downstream tasks in our dataset, and show that IDS is also effective in natural imagery domains by demonstrating performance over CIFAR-10 [17].

In summary, our paper contributions are:

1. We adapt implicit data synthesis to contrastive learning, replacing data-space augmentation with per-forward-pass perturbation of a single fully-connected layer in the encoder.
2. We evaluate the method on synthetic meteor radar observations, a setting in which canonical SimCLR augmentations corrupt the underlying physical signal, and show that IDS matches or outperforms a flip-and-rotation baseline across CNN encoders.
3. We verify that the technique generalizes beyond the radar domain by reproducing the comparison on CIFAR-10 under a matched (flip-and-rotation) augmentation budget, and characterize the sensitivity of the method to the perturbation scale  $s_l$ .

## 2 Related work

Modern self-supervised learning for visual representations is dominated by joint-embedding methods that learn invariances by aligning two views of the same sample. SimCLR [3] establishes the canonical

---

<sup>1</sup>Though pairwise contrastive losses are common, others are available—see *e.g.* [14] and [1].

recipe of random crop, color jitter, and Gaussian blur trained against an NT-Xent loss; MoCo [8] replaces the in-batch negatives with a momentum-encoded queue; BYOL [7] and SimSiam [4] dispense with negatives entirely, relying on a predictor network and asymmetric stop-gradient to avoid representational collapse. More recent work shifts to self-distillation with vision transformers (*e.g.* the DINO family [2, 19, 21]) and to masked reconstruction (*e.g.* MAE [9]). Across all of these methods the view-generation step is essentially unchanged from SimCLR: positive pairs are produced by stochastic data-space augmentation. Our contribution is orthogonal to the choice of objective—the perturbation we introduce in Section 3 can in principle be plugged into any of these frameworks—and we adopt the SimCLR setting because it isolates the view-generation mechanism most cleanly.

Mechanically, IDS resembles a long line of stochastic-forward-pass methods. Dropout [22] and DropConnect [23] inject multiplicative Bernoulli noise into activations and weights respectively; stochastic depth [13] randomly skips entire residual blocks; and Bayesian treatments such as MC dropout [5] and SWAG [18] interpret stochastic forward passes as samples from an approximate weight posterior, used at inference time for uncertainty quantification. In all of these, the noise serves either as a regularizer during training or as a posterior sampling mechanism at test time; the loss is computed on a single noisy forward pass.

IDS uses the same mechanism for a different purpose: two *independent* stochastic forward passes on the same input produce a positive pair for a contrastive loss, and the noise is the sole source of view variation rather than a regularizer layered on top of data-space augmentation. The closest precedent is SimCSE [6], which uses independently sampled dropout masks to construct positive pairs for contrastive sentence embedding—demonstrating that stochastic forward passes *can* substitute for data-space augmentation in a contrastive setting, but doing so via Bernoulli activation masks on a Transformer backbone, in a domain (text) where the analogue of crop-and-flip is poorly defined to begin with. We extend this idea to image contrastive learning with additive Gaussian perturbation of weights at a designated layer, motivated by scientific imaging domains in which the standard data-space augmentations corrupt the underlying physical signal.

A natural comparison is also the variational autoencoder [16], whose encoder defines a distribution  $q(z | x)$  from which multiple latents can be sampled for a single input. IDS differs in where the stochasticity lives—we sample a random encoder  $f_{\theta+\lambda}$  from a fixed distribution over functions rather than sampling latents from a learned, input-dependent distribution—and has no decoder, reconstruction term, or KL penalty shaping the perturbation scale.

### 3 Methodology

Implicit data synthesis is implemented by adding a noise term to the standard formulation for a Multilayer Perceptron (MLP):

$$\mathbf{h}^{(l)} = \sigma((W^{(l)} + \lambda^{(l)})\mathbf{h}^{(l-1)}) \quad (1)$$

where  $\mathbf{h}^{(l)}$  is layer  $l$ 's activation,  $\mathbf{h}^{(l-1)}$  is the previous layer's activation,  $W^{(l)}$  are layer  $l$ 's weights, and  $\lambda^{(l)}$  is a perturbation matrix of the same shape as  $W^{(l)}$ . The entries of  $\lambda^{(l)}$  are sampled i.i.d. from  $\mathcal{N}(0, s_l)$ , where  $s_l$  is a per-layer scale hyperparameter. The perturbation is resampled on every forward pass; the underlying weights  $W^{(l)}$  are unaffected and are updated only through the contrastive loss. The geometric intuition for this is that perturbations in weight space induce a distribution over functions, which induces a distribution over the representations of the samples.

The weight-perturbation operator in Equation 1 is adapted from Wasserstein-Distributed Outlier Exposure (W-DOE) [24], which uses perturbations of network weights to synthesize auxiliary out-of-distribution (OOD) samples for outlier exposure training. In W-DOE, the perturbation expands the support of an auxiliary OOD set used in a supervised binary in-distribution-vs-OOD objective; the perturbed forward passes serve as additional negative examples whose distance from the in-distribution manifold is bounded by the Wasserstein radius induced by  $s_l$ . We retain the perturbation mechanism but apply it in a fundamentally different role: rather than generating negatives against a fixed in-distribution density, two independent draws of  $\lambda$  are used to generate a positive pair for a self-supervised contrastive objective. The two settings share the geometric intuition that small weight perturbations induce bounded movements in representation space, but they differ in what that bounded movement is used for—bounding the OOD synthesis radius in W-DOE, and bounding the

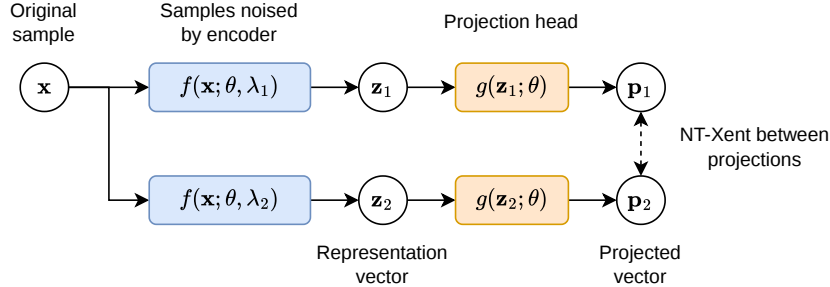


Figure 1: Diagram showing the contrastive IDS architecture. Note that, as opposed to SimCLR, there is no data-space augmentation block—rather, the augmentations are derived from the noise term  $\lambda$  parameterizing the encoder network  $f(\cdot)$ .

intra-class spread of synthesized positives. Consequently, the W-DOE convergence and bound results, which are stated for the OOD-exposure objective, do not transfer directly to the NT-Xent setting, and we treat the perturbation as a heuristic augmentation operator rather than one with inherited theoretical guarantees.

Within the SimCLR framework, this perturbation provides the mechanism for constructing positive pairs. Given an input  $\mathbf{x}$ , two independent draws  $\lambda_1^{(l)}, \lambda_2^{(l)} \sim \mathcal{N}(0, s_l)$  yield two perturbed encoders  $f_{\lambda_1}$  and  $f_{\lambda_2}$ , and the positive pair is  $(\hat{\mathbf{x}}_1, \hat{\mathbf{x}}_2) = (f_{\lambda_1}(\mathbf{x}), f_{\lambda_2}(\mathbf{x}))$ . The two views are then projected and scored under the standard NT-Xent loss in the same manner as SimCLR; only the source of view variation has changed. Because the input  $\mathbf{x}$  is passed through the network unmodified, no data-space augmentation is required, and the augmentation does not need to be designed against the physical structure of the data. The resulting configuration is shown in Figure 1.

The  $\lambda^{(l)}$  perturbation is not applied uniformly across the network. In practice,  $s_l$  is set to zero for all but a small number of layers, restricting the weight-space augmentation to a single, well-defined site. The choice of which layers to perturb is left as a design parameter. In this work, the perturbation is applied at the first fully-connected layer following the convolutional stack (see Section 5). Restricting perturbation to a representation-space layer rather than to the convolutional features keeps the augmentation acting on already-abstracted features. Perturbing in feature space yields samples that remain close to the data manifold, whereas perturbing earlier layers risks destroying low-level structure that the encoder has not yet learned to ignore.

The scale parameter  $s_l$  controls the effective spread of the synthesized positives. With  $s_l = 0$  the two views collapse to the same point and the contrastive loss becomes degenerate: as  $s_l$  grows the two views become arbitrarily dissimilar and the encoder is asked to embed unrelated points together, which destabilizes training.  $s_l$  thus plays a role analogous to augmentation strength in standard SimCLR, and we treat it as a hyperparameter to be swept (Section 5). At evaluation time, we set  $s_l = 0$  in all layers, recovering a deterministic encoder.

## 4 Experimental Setup

To validate the efficacy of implicit data synthesis within the contrastive framework, we utilize a dataset of synthetically-generated radar samples containing simulated meteor head echo observations. Since radar observations of meteor head echoes can be simulated in a computationally efficient manner via various physical approximations that preserve realism [11], this synthetic data closely mirrors real-world distributions while providing a high-volume testbed for our representation learning pipeline. Examples of synthetic radar data samples, along with the pixel-wise labels indicating meteor head echoes, are shown in Figure 2.

We crop down the synthetic observations (originally  $512 \times 512$  images) to a set of  $N \times N$  subtiles, allowing us to evaluate the spatial resolution bounds of the learned representations and assess how varying amounts of spatial context affect the contrastive learning process.

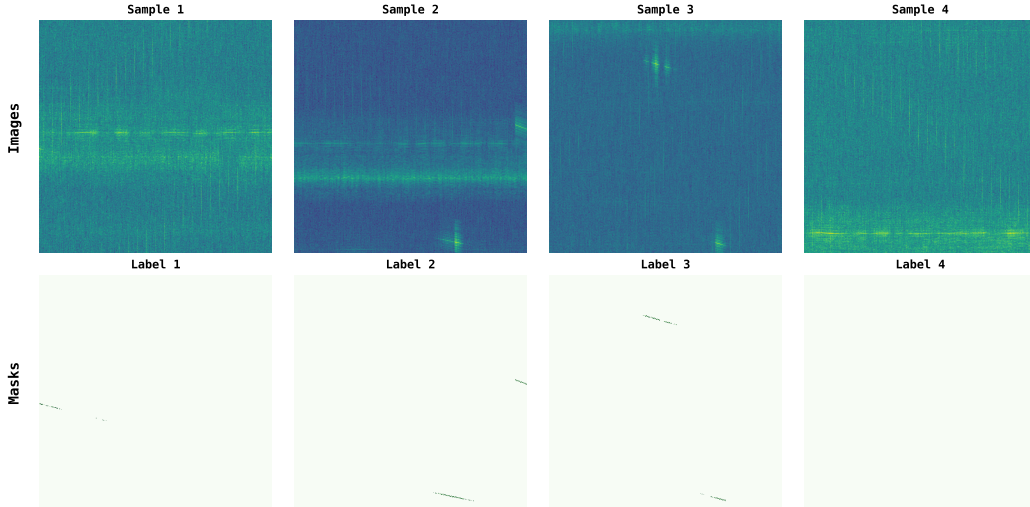


Figure 2: A selection of synthetic radar data samples and associated per-pixel labels indicating meteor locations.

To establish a performance baseline, models are trained utilizing standard data-space augmentations. Specifically, random horizontal/vertical flips and rotations. This baseline represents the standard approach in the literature and serves as the comparative benchmark against our proposed implicit data synthesis technique.

#### 4.1 Evaluation

To evaluate the quality of the learned representations, we freeze the encoder weights post-training, set the  $s_l$  to zero in all layers, and remove the projection head. We train both a shallow MLP classifier (a linear probe) as well as a  $k$ -nearest-neighbor classifier on the resulting embeddings, evaluated against a binary classification problem: determining whether a meteor head echo exists in a given sample. The performance of this probe serves as our primary metric for the semantic richness of the unsupervised latent space. Comparing the  $k$ -NN and MLP performance allows us to evaluate both the local clustering and the broader linear separability of the learned representations.

#### 4.2 Model Architectures

We evaluate the representation learning pipeline across a spectrum of encoder architectures to assess both scalability and capacity requirements. The evaluated base models include a series of simple Convolutional Neural Networks (CNNs) explicitly scaled for varying input tile sizes ( $8 \times 8$  through  $256 \times 256$ ) paired with MLP layers (which receive the noise), as well as standard ResNet-18 and ResNet-50 architectures. The ResNets are evaluated exclusively on the  $256 \times 256$  tiles, and again only the fully-connected MLP layers receive noise.

All CNN encoders follow a common template: a stack of conv2d–ReLU–maxpool2d blocks followed by a two-layer MLP that produces a representation vector of dimension  $D_r = 32$ . The number of convolutional blocks, the kernel sizes, and the pooling strides are scaled with the input tile size so that the spatial extent collapses to a  $3 \times 3$  feature map prior to flattening. The smallest two variants (CNN- $8 \times 8$  and CNN- $16 \times 16$ ) use two convolutional blocks with  $2 \times 2$  pooling; the mid-sized variants (CNN- $32 \times 32$  through CNN- $64 \times 64$ ) retain two blocks but increase the kernel size and pooling stride; and the largest variants (CNN- $128 \times 128$  and CNN- $256 \times 256$ ) use three convolutional blocks. Channel widths grow with depth, ranging from 16–32 channels in the smallest model up to 32–64–128 in the largest. Across all CNN variants the channel counts and the MLP hidden sizes are kept small relative to the ResNet baselines, in order to isolate the effect of input resolution from raw model capacity.

For all encoders—CNN and ResNet alike—the standard SimCLR projection head is attached to the representation vector: a two-layer MLP with a ReLU nonlinearity that maps from  $\mathbb{R}^{D_r}$  to a projection

space of dimension  $D_p = 16$ . For the ResNet backbones, the default classification head is replaced with an identity layer so that the backbone outputs its native feature dimension (512 for ResNet-18, 2048 for ResNet-50) directly into the projection MLP. The contrastive loss is computed in projection space, while the downstream linear probe and  $k$ -NN classifier operate on the representation vector  $\mathbf{h} \in \mathbb{R}^{D_r}$  obtained immediately before the projection head.

When implicit data synthesis is enabled, the perturbation  $\lambda$  is applied only to the weights of the first fully-connected layer of the encoder’s MLP head (*i.e.*, fc1 in the CNN variants). All convolutional weights and the projection head remain unperturbed. This restricts the weight-space augmentation to a single, well-defined site in the network and keeps the perturbation budget comparable across architectures of differing depth.

### 4.3 Baselines

To assess the efficacy of implicit data synthesis as a contrastive augmentation strategy, we compare against three baseline configurations, designed to isolate both the in-domain performance on meteor radar data and the generality of the technique across data modalities: a direct application of natural imagery augmentation to the radar dataset, an in-domain augmentation applied to the radar dataset, and a comparison to CIFAR-10 with both a matching set of baseline augmentations and IDS applied.

The first two baselines target our primary dataset directly. First, we train a SimCLR pipeline on the synthetic meteor observations using a restricted set of data-space augmentations: random horizontal/vertical flips and rotations. We deliberately omit the remainder of the canonical SimCLR augmentation suite [3]—in particular, color jitter and aggressive cropping—as these operations do not compare cleanly against implicit data synthesis on radar data because they would corrupt the underlying physical signal rather than produce a semantically equivalent view. This configuration provides a direct point of comparison against our proposed method, in which the same encoder is trained using only implicit data synthesis (*i.e.*, weight-space perturbation) as the source of positive-pair variation. The contrast between these two configurations isolates the effect of replacing data-space augmentations with representation-space perturbations on a domain in which natural imagery augmentations are not physically well-motivated.

Additionally, we evaluate an in-domain, physics-motivated augmentation strategy tailored to the structure of meteor radar observations. Each synthetic sample is transformed via a column-wise FFT, and a contiguous band of the resulting spectrum (set to 15%) is zeroed out before the inverse transform is applied to recover a perturbed sample in the original domain. The masked band is selected randomly per sample, yielding two distinct views when applied twice to the same input. This augmentation is used as the sole source of positive-pair variation; no flips, rotations, or other data-space perturbations are composed with it. The motivation is to produce views that differ in their frequency content while preserving the spatial and temporal structure of the underlying radar signal, providing a domain-appropriate point of comparison against both the flip-and-rotation baseline and implicit data synthesis.

The remaining two baselines are designed to demonstrate that implicit data synthesis generalizes beyond radar observations to natural imagery. To this end, we repeat the above pair of experiments on the CIFAR-10 [17] dataset: one configuration trained using the same flip-and-rotation augmentation set, and a second trained using implicit data synthesis in place of those augmentations. To maintain parity with the binary classification protocol used for the meteor radar evaluation, we collapse the ten CIFAR-10 classes into two superclasses: *vehicle* (airplane, automobile, ship, truck) and *animal* (bird, cat, deer, dog, frog, horse). CIFAR-10 thus serves as a natural imagery testbed where the contrastive learning protocol is well-characterized, and allows us to verify that the gains observed on meteor data are not an artifact of the radar domain.

Across all of the above configurations, we hold the encoder architecture, projection head, optimizer, batch size, and number of training epochs fixed, varying only the augmentation strategy. Downstream evaluation follows the protocol described in Section 4.2: encoder weights are frozen,  $s_l$  is set to zero, the projection head is removed, and both a linear probe and a  $k$ -NN classifier are trained on the resulting embeddings.

## 5 Results

We report linear-probe and  $k$ -NN classification accuracy across three augmentation conditions: the flip-and-rotation baseline, the in-domain FFT masking augmentation, and IDS. Each condition is evaluated on the synthetic meteor dataset across the six CNN variants and the two ResNet backbones described in Section 4.2, and on CIFAR-10 across the same encoder set. All runs are repeated at minimum three times with different seeds (varying per experiment); we report the mean and standard deviation of the resulting accuracies. The sensitivity of IDS to  $s_l$  is examined separately on CNN-16 $\times$ 16 in Figure 3.

Table 1: Top-line model accuracy on meteor classification across baseline, in-domain (FFT), and IDS noising schemes, with the best performance bolded. The classification task was evaluated as described in Section 4.1. All models were run 3 times with  $s_l = 0.02$  for an identical number of epochs. Mean and standard deviation are reported.

| MLP (%)              |                                    |                                    |                                    |
|----------------------|------------------------------------|------------------------------------|------------------------------------|
| Model                | Baseline                           | In-domain                          | IDS                                |
| CNN-8 $\times$ 8     | 83.50 $\pm$ 1.41                   | 80.67 $\pm$ 1.18                   | <b>84.50 <math>\pm</math> 0.41</b> |
| CNN-16 $\times$ 16   | 80.83 $\pm$ 1.65                   | 71.67 $\pm$ 1.31                   | <b>85.17 <math>\pm</math> 1.43</b> |
| CNN-32 $\times$ 32   | 77.33 $\pm$ 0.85                   | 74.67 $\pm$ 1.65                   | <b>78.00 <math>\pm</math> 0.00</b> |
| CNN-64 $\times$ 64   | 75.83 $\pm$ 0.24                   | 74.33 $\pm$ 1.03                   | <b>76.67 <math>\pm</math> 0.47</b> |
| CNN-128 $\times$ 128 | <b>75.17 <math>\pm</math> 0.47</b> | 51.67 $\pm$ 0.94                   | 73.83 $\pm$ 1.25                   |
| CNN-256 $\times$ 256 | 66.50 $\pm$ 1.22                   | 52.83 $\pm$ 0.62                   | <b>71.17 <math>\pm</math> 0.24</b> |
| ResNet-18            | 87.17 $\pm$ 0.62                   | <b>93.67 <math>\pm</math> 1.03</b> | 86.50 $\pm$ 0.41                   |
| ResNet-50            | 92.17 $\pm$ 0.24                   | 93.67 $\pm$ 0.62                   | <b>94.33 <math>\pm</math> 0.47</b> |
| $k$ -NN (%)          |                                    |                                    |                                    |
| Model                | Baseline                           | In-domain                          | IDS                                |
| CNN-8 $\times$ 8     | <b>84.50 <math>\pm</math> 0.41</b> | 80.67 $\pm$ 0.62                   | 84.00 $\pm$ 0.41                   |
| CNN-16 $\times$ 16   | 77.83 $\pm$ 0.47                   | 75.83 $\pm$ 1.65                   | <b>81.67 <math>\pm</math> 0.24</b> |
| CNN-32 $\times$ 32   | 76.67 $\pm$ 2.01                   | 73.83 $\pm$ 0.24                   | <b>77.17 <math>\pm</math> 0.94</b> |
| CNN-64 $\times$ 64   | 77.33 $\pm$ 0.85                   | 79.00 $\pm$ 2.12                   | <b>79.67 <math>\pm</math> 2.01</b> |
| CNN-128 $\times$ 128 | 75.83 $\pm$ 1.03                   | 54.17 $\pm$ 0.62                   | <b>83.33 <math>\pm</math> 1.03</b> |
| CNN-256 $\times$ 256 | 72.33 $\pm$ 0.85                   | 57.67 $\pm$ 6.60                   | <b>80.17 <math>\pm</math> 0.94</b> |
| ResNet-18            | 82.50 $\pm$ 2.12                   | <b>90.17 <math>\pm</math> 0.47</b> | 80.33 $\pm$ 2.25                   |
| ResNet-50            | 88.33 $\pm$ 0.62                   | <b>92.50 <math>\pm</math> 0.82</b> | 86.00 $\pm$ 1.08                   |

Table 1 reports linear-probe and  $k$ -NN accuracy on the synthetic meteor dataset across the CNN and ResNet encoders. On the CNN backbones, IDS matches or outperforms the flip-and-rotation baseline at every input resolution under both probes, with the largest gains appearing at the higher resolutions. The pattern reverses on the ResNet backbones, where the in-domain FFT augmentation largely yields the best performance and IDS underperforms the flip-and-rotation baseline, particularly on ResNet-18 under the linear probe. We return to this in Section 6.

On CIFAR-10 (Table 2), IDS improves over the flip-and-rotation baseline on seven of eight encoder-probe combinations. We emphasize that this comparison is deliberately restricted: to maintain parity with the meteor radar augmentation protocol, both conditions use only flips and rotations rather than the full SimCLR augmentation suite [17], which includes random resized crop, color jitter, and grayscale conversion. Under that stronger protocol, canonical SimCLR augmentations are known to substantially outperform flip-and-rotation alone on CIFAR-10, and we make no claim that IDS competes with a well-tuned data-space augmentation pipeline on natural imagery. The CIFAR-10 result is therefore best read as evidence that IDS is not specific to the radar domain—*i.e.*, that weight-space perturbation produces useful view variation under matched augmentation budgets—rather than as evidence that IDS is preferable to data-space augmentation where the latter is physically well-motivated.

Figure 3 sweeps the perturbation scale  $s_l$  on CNN-16 $\times$ 16 from 0.01 to 0.20. Performance is broadly insensitive to the choice of  $s_l$  across this range: the linear probe varies between 0.78 and 0.82 and the  $k$ -NN probe between 0.77 and 0.80, with a sharp optimum. We did not observe the training

Table 2: Accuracy over CIFAR-10 across baseline and IDS noising schemes, with the best performance bolded. See Section 4.3 for experimental configuration. All models were run 3 times with  $s_l = 0.02$  for an identical number of epochs.

| MLP (%)     |              |                     |
|-------------|--------------|---------------------|
| Model       | Baseline     | IDS                 |
| CNN-8×8     | 66.50 ± 0.82 | <b>74.33 ± 1.55</b> |
| CNN-16×16   | 62.17 ± 0.62 | <b>71.17 ± 0.85</b> |
| CNN-32×32   | 62.83 ± 1.65 | <b>74.33 ± 3.40</b> |
| CNN-64×64   | 62.83 ± 0.62 | <b>71.17 ± 0.62</b> |
| CNN-128×128 | 61.67 ± 0.62 | <b>68.67 ± 0.24</b> |
| CNN-256×256 | 64.67 ± 2.36 | <b>70.33 ± 1.18</b> |
| ResNet-18   | 86.17 ± 0.24 | <b>87.17 ± 0.85</b> |
| ResNet-50   | 80.67 ± 0.62 | <b>82.50 ± 0.41</b> |

| $k$ -NN (%) |              |                     |
|-------------|--------------|---------------------|
| Model       | Baseline     | IDS                 |
| CNN-8×8     | 64.67 ± 0.24 | <b>71.17 ± 0.24</b> |
| CNN-16×16   | 64.17 ± 0.24 | <b>71.50 ± 1.78</b> |
| CNN-32×32   | 65.00 ± 1.08 | <b>74.00 ± 1.08</b> |
| CNN-64×64   | 65.00 ± 0.00 | <b>71.17 ± 0.62</b> |
| CNN-128×128 | 63.83 ± 1.25 | <b>72.17 ± 0.62</b> |
| CNN-256×256 | 64.50 ± 1.22 | <b>77.00 ± 1.08</b> |
| ResNet-18   | 82.67 ± 0.94 | <b>84.50 ± 0.41</b> |
| ResNet-50   | 76.33 ± 0.47 | <b>80.83 ± 0.62</b> |

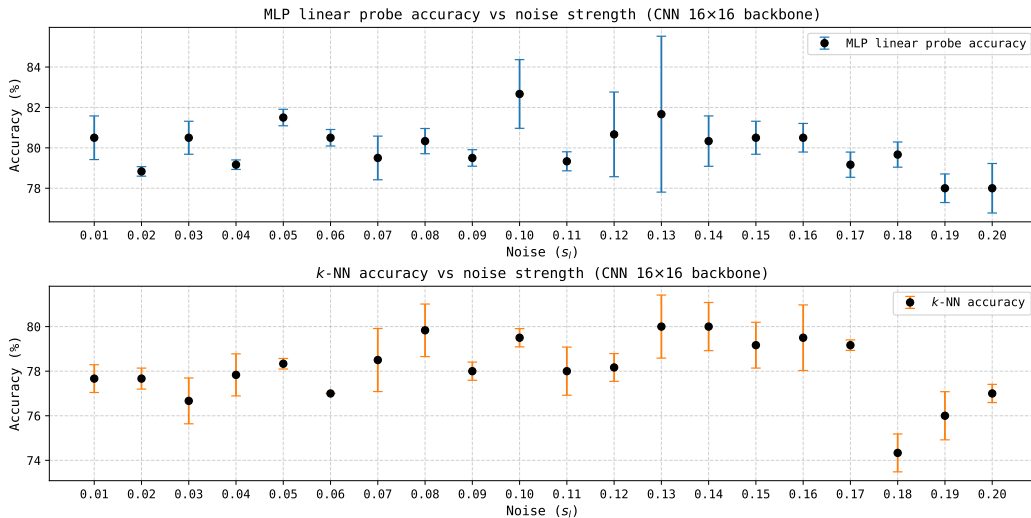


Figure 3: Noise sweep across CNN-16×16 architecture reporting accuracy on meteor classification with both the MLP linear probe and  $k$ -NN accuracy, evaluated as in Section 4.2. All models were run 5 times for an identical number of epochs. Mean and standard deviation are reported.

instability predicted at large  $s_l$  within the swept range, suggesting that for this architecture the useful range of  $s_l$  extends well beyond the value used in Tables 1 and 2.

## 6 Discussion

The meteor dataset results support the central claim of the paper in a restricted form. On the CNN encoders, replacing data-space augmentations with weight-space perturbation produces representations of comparable or better linear separability and local clustering, without requiring augmentations that may corrupt the underlying physical signal. The CIFAR-10 results indicate that this behavior is not specific to the radar domain.

The ResNet results on meteor radar are the clearest qualification. Applying IDS at a single fully-connected layer after a much deeper convolutional stack appears to under-perturb the representation; the bulk of the encoder’s capacity sits upstream of the perturbation site, and the resulting view variation is presumably too small to drive the contrastive objective. This is consistent with the design choice—perturbing one layer to keep the budget comparable across architectures—failing to scale with depth. A natural next step is to either widen the set of perturbed layers in deeper backbones or to scale  $s_l$  with the receptive field downstream of the perturbation site. This is left to future work.

The flatness of the  $s_l$  sweep is also worth noting. The theoretical account in Section 3 predicts degeneracy at  $s_l = 0$  and instability at large  $s_l$ , with a useful regime in between. We observe the lower bound but not the upper, at least on CNN-16×16 up to  $s_l = 0.20$ . Whether this reflects a property of the architecture, the dataset, or the single-layer perturbation site cannot be easily discerned from the present experiments.

## 7 Conclusion

We have presented implicit data synthesis as a contrastive augmentation strategy that operates in weight space rather than data space, and evaluated it against flip-and-rotation baselines on synthetic meteor radar observations and on CIFAR-10. On the shallow CNN encoders, IDS matches or outperforms the baseline on both datasets. On the deeper ResNet backbones applied to meteor data, single-site perturbation is insufficient and the baseline augmentations remain preferable. The technique is most useful in the setting it was designed for: domains where data-space augmentations are not physically well-motivated. Extending the analysis to multi-site perturbation, to additional scientific imaging modalities, and to a characterization of the upper bound on  $s_l$  are clear directions for follow-up work.

## Acknowledgments

The authors graciously thank Sigrid Elschot and Nicolas Lee for their efforts towards experiment planning and data analysis at Stanford University, Marco Milla and Karim Kuyeng Ruiz for their assistance in data collection at Jicamarca Radio Observatory, and Lindsey Marinello at the Georgia Institute of Technology for her generous help with the manuscript. This work was supported by NSF Grants 1920383, 2048349, and 2301645.

## References

- [1] M. Caron, I. Misra, J. Mairal, P. Goyal, P. Bojanowski, and A. Joulin. Unsupervised Learning of Visual Features by Contrasting Cluster Assignments, Jan. 2021.
- [2] M. Caron, H. Touvron, I. Misra, H. Jégou, J. Mairal, P. Bojanowski, and A. Joulin. Emerging Properties in Self-Supervised Vision Transformers, Apr. 2021.
- [3] T. Chen, S. Kornblith, M. Norouzi, and G. Hinton. A Simple Framework for Contrastive Learning of Visual Representations, June 2020.
- [4] X. Chen and K. He. Exploring Simple Siamese Representation Learning, Nov. 2020.
- [5] Y. Gal and Z. Ghahramani. Dropout as a Bayesian Approximation: Representing Model Uncertainty in Deep Learning, June 2015.

- [6] T. Gao, X. Yao, and D. Chen. SimCSE: Simple Contrastive Learning of Sentence Embeddings, Apr. 2021.
- [7] J.-B. Grill, F. Strub, F. Altché, C. Tallec, P. H. Richemond, E. Buchatskaya, C. Doersch, B. A. Pires, Z. D. Guo, M. G. Azar, B. Piot, K. Kavukcuoglu, R. Munos, and M. Valko. Bootstrap your own latent: A new approach to self-supervised Learning, Sept. 2020.
- [8] K. He, H. Fan, Y. Wu, S. Xie, and R. Girshick. Momentum Contrast for Unsupervised Visual Representation Learning, Mar. 2020.
- [9] K. He, X. Chen, S. Xie, Y. Li, P. Dollár, and R. Girshick. Masked Autoencoders Are Scalable Vision Learners, Nov. 2021.
- [10] T. Hedges, N. Lee, and S. Elschot. Meteor Head Echo Analyses From Concurrent Radar Observations at AMISR Resolute Bay, Jicamarca, and Millstone Hill. *Journal of Geophysical Research: Space Physics*, 127(10):e2022JA030709, Oct. 2022. ISSN 2169-9380, 2169-9402. doi: 10.1029/2022JA030709.
- [11] T. Hedges, N. Lee, and S. Elschot. Meteor Head Echo Detection at Multiple High-Power Large-Aperture Radar Facilities via a Convolutional Neural Network Trained on Synthetic Radar Data. *Journal of Geophysical Research: Space Physics*, 129(4):e2023JA032204, Apr. 2024. ISSN 2169-9380, 2169-9402. doi: 10.1029/2023JA032204.
- [12] H. Hu, X. Wang, Y. Zhang, Q. Chen, and Q. Guan. A comprehensive survey on contrastive learning. *Neurocomputing*, 610:128645, Dec. 2024. ISSN 0925-2312. doi: 10.1016/j.neucom.2024.128645.
- [13] G. Huang, Y. Sun, Z. Liu, D. Sedra, and K. Weinberger. Deep Networks with Stochastic Depth, Mar. 2016.
- [14] P. Kage and P. Andreadis. Multi-modal, Multi-scale Representation Learning for Satellite Imagery Analysis Just Needs a Good ALiBi. In *4th Space Imaging Workshop*, Space Exploration Analysis Laboratory, Georgia Institute of Technology, Oct. 2024.
- [15] P. Kage, J. C. Rothenberger, P. Andreadis, and D. I. Diochnos. A Review of Pseudo-Labeling for Computer Vision, May 2025.
- [16] D. P. Kingma and M. Welling. Auto-Encoding Variational Bayes. *arXiv:1312.6114 [cs, stat]*, May 2014.
- [17] A. Krizhevsky, V. Nair, and G. Hinton. CIFAR-10 (canadian institute for advanced research). 2009.
- [18] W. J. Maddox, P. Izmailov, T. Garipov, D. Vetrov, and A. G. Wilson. A simple baseline for bayesian uncertainty in deep learning. In H. Wallach, H. Larochelle, A. Beygelzimer, F. dAlché-Buc, E. Fox, and R. Garnett, editors, *Advances in Neural Information Processing Systems*, volume 32. Curran Associates, Inc., 2019.
- [19] M. Oquab, T. Darcet, T. Moutakanni, H. Vo, M. Szafraniec, V. Khalidov, P. Fernandez, D. Haziza, F. Massa, A. El-Nouby, M. Assran, N. Ballas, W. Galuba, R. Howes, P.-Y. Huang, S.-W. Li, I. Misra, M. Rabbat, V. Sharma, G. Synnaeve, H. Xu, H. Jegou, J. Mairal, P. Labatut, A. Joulin, and P. Bojanowski. DINOv2: Learning Robust Visual Features without Supervision, Apr. 2023.
- [20] C. Shorten and T. M. Khoshgoftaar. A survey on Image Data Augmentation for Deep Learning. *Journal of Big Data*, 6(1):60, Dec. 2019. ISSN 2196-1115. doi: 10.1186/s40537-019-0197-0.
- [21] O. Siméoni, H. V. Vo, M. Seitzer, F. Baldassarre, M. Oquab, C. Jose, V. Khalidov, M. Szafraniec, S. Yi, M. Ramamonjisoa, F. Massa, D. Haziza, L. Wehrstedt, J. Wang, T. Darcet, T. Moutakanni, L. Sentana, C. Roberts, A. Vedaldi, J. Tolan, J. Brandt, C. Couprie, J. Mairal, H. Jégou, P. Labatut, and P. Bojanowski. DINOv3, Aug. 2025.
- [22] N. Srivastava, G. Hinton, A. Krizhevsky, I. Sutskever, and R. Salakhutdinov. Dropout: A Simple Way to Prevent Neural Networks from Overfitting. *Journal of Machine Learning Research*, 15, 2014.

- [23] L. Wan, M. Zeiler, S. Zhang, Y. Le Cun, and R. Fergus. Regularization of neural networks using DropConnect. In S. Dasgupta and D. McAllester, editors, *Proceedings of the 30th International Conference on Machine Learning*, volume 28 of *Proceedings of Machine Learning Research*, pages 1058–1066, Atlanta, Georgia, USA, June 2013. PMLR.
- [24] Q. Wang, B. Han, Y. Liu, C. Gong, T. Liu, and J. Liu. W-DOE: Wasserstein Distribution-Agnostic Outlier Exposure. *IEEE Transactions on Pattern Analysis and Machine Intelligence*, 47(5):3530–3545, May 2025. ISSN 1939-3539. doi: 10.1109/TPAMI.2025.3531000.

## **A Technical appendices and supplementary material**

All experiments were run on a single NVIDIA DGX Spark, and took approximately seven days to complete.